



HAL
open science

Serial crystallography captures dynamic control of sequential electron and proton transfer events in a flavoenzyme

Manuel Maestre-Reyna, Cheng-Han Yang, Eriko Nango, Wei-Cheng Huang, Eka Putra Gusti Ngurah Putu, Wen-Jin Wu, Po-Hsun Wang, Sophie Franz-Badur, Martin Saft, Hans-Joachim Emmerich, et al.

► **To cite this version:**

Manuel Maestre-Reyna, Cheng-Han Yang, Eriko Nango, Wei-Cheng Huang, Eka Putra Gusti Ngurah Putu, et al.. Serial crystallography captures dynamic control of sequential electron and proton transfer events in a flavoenzyme. *Nature Chemistry*, 2022, 14 (6), pp.677-685. 10.1038/s41557-022-00922-3 . hal-03716098

HAL Id: hal-03716098

<https://hal.science/hal-03716098v1>

Submitted on 1 Sep 2022

HAL is a multi-disciplinary open access archive for the deposit and dissemination of scientific research documents, whether they are published or not. The documents may come from teaching and research institutions in France or abroad, or from public or private research centers.

L'archive ouverte pluridisciplinaire **HAL**, est destinée au dépôt et à la diffusion de documents scientifiques de niveau recherche, publiés ou non, émanant des établissements d'enseignement et de recherche français ou étrangers, des laboratoires publics ou privés.

1 **Serial crystallography captures dynamic control of sequential electron and proton**
2 **transfer events in a flavoenzyme**

3

4 Manuel Maestre-Reyna¹, Cheng-Han Yang¹, Eriko Nango^{2,3}, Wei-Cheng Huang¹, Eka Putra
5 Gusti Ngurah Putu¹, Wen-Jin Wu¹, Po-Hsun Wang¹, Sophie Franz-Badur⁴, Martin Saft⁴, Hans-
6 Joachim Emmerich⁴, Hsiang-Yi Wu¹, Cheng-Chung Lee¹, Kai-Fa Huang¹, Yao-Kai Chang¹,
7 Jiahn-Haur Liao¹, Jui-Hung Weng¹, Wael Gad¹, Chiung-Wen Chang¹, Allan H. Pang¹,
8 Michihiro Sugahara², Shigeki Owada⁵, Yuhei Hosokawa⁶, Yasumasa Joti^{2,5}, Ayumi
9 Yamashita^{2,3}, Rie Tanaka^{2,3}, Tomoyuki Tanaka^{2,3}, Luo Fangjia^{2,3}, Kensuke Tono⁵, Kai-Cheng
10 Hsu⁷, Stephan Kiontke⁴, Igor Schapiro⁸, Roberta Spadacini⁹, Antoine Royant^{10,11}, Junpei
11 Yamamoto⁶, So Iwata^{2,3}, Lars-Oliver Essen^{4,12,*}, Yoshitaka Bessho^{1,2,*}, Ming-Daw Tsai^{1,13,*}

12 **Affiliations:**

13 ¹Institute of Biological Chemistry, Academia Sinica, 128 Academia Rd. Sec. 2, Nankang,
14 Taipei, 115, Taiwan.

15 ²RIKEN SPring-8 Center, 1-1-1 Kouto, Sayo, Hyogo, 679-5148, Japan.

16 ³Department of Cell Biology, Graduate School of Medicine, Kyoto University, Yoshidakonoe-
17 cho, Sakyo-ku, Kyoto, 606-8501, Japan.

18 ⁴Department of Chemistry, Philipps University Marburg, Hans-Meerwein Strasse 4, Marburg
19 35032, Germany.

20 ⁵Japan Synchrotron Radiation Research Institute, 1-1-1 Kouto, Sayo, Hyogo, 679-5198, Japan.

21 ⁶Division of Chemistry, Graduate School of Engineering Science, Osaka University, 1-3
22 Machikaneyama, Toyonaka, Osaka 560-8531, Japan.

23 ⁷Graduate Institute of Cancer Biology and Drug Discovery, College of Medical Science and
24 Technology, Taipei Medical University, Taipei, Taiwan

25 ⁸Fritz Haber Center for Molecular Dynamics, Institute of Chemistry
26 The Hebrew University of Jerusalem, Jerusalem 91904, Israel

27 ⁹Dipartimento di Scienze e tecnologie, Università degli studi del Sannio, Benevento, Italy.

28 ¹⁰Institut de Biologie Structurale (IBS), University Grenoble Alpes, CNRS, CEA, 38044
29 Grenoble, France.

30 ¹¹European Synchrotron Radiation Facility, 38043 Grenoble, France.

31 ¹²Center of Synthetic Microbiology, Philipps University Marburg, Hans-Meerwein Straße 4,
32 35032 Marburg, Germany.

33 ¹³Institute of Biochemical Sciences, National Taiwan University, 1, Roosevelt Rd. Sec. 4,
34 Taipei 106, Taiwan.

35

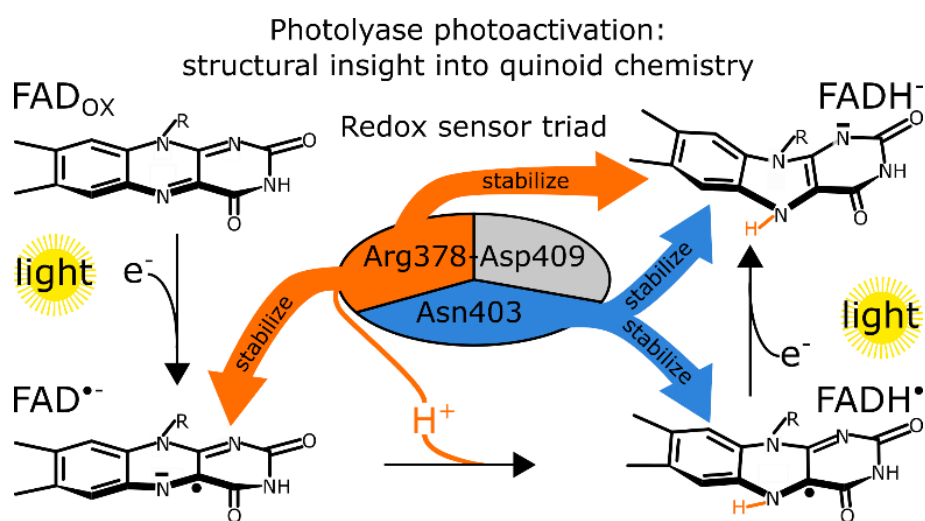
36 ***e-mail:** mdsai@gate.sinica.edu.tw ; bessho@sinica.edu.tw ; essen@chemie.uni-marburg.de

37

38 **Abstract**

39 **Flavin coenzymes are universally found in biological redox reactions. DNA photolyases**
40 **with their flavin chromophore (FAD) utilize blue light for DNA repair and**
41 **photoreduction.** The latter process involves two single-electron transfers to FAD with an
42 **intermittent protonation step to prime the enzyme active for DNA repair. Here we use**
43 **time-resolved serial femtosecond X-ray crystallography to describe how light-driven**
44 **electron transfers trigger subsequent nanosecond-to-microsecond entanglement between**
45 **FAD and its Asn/Arg-Asp redox sensor triad. We found that this key feature within the**
46 **photolyase-cryptochrome family regulates FAD re-hybridization and protonation. After**
47 **first electron transfer, the FAD^{•-} isoalloxazine ring *twists strongly* when the arginine**
48 **closes in to stabilize the negative charge. Subsequent breakage of the arginine-aspartate**
49 **salt bridge promotes proton transfer from arginine to FAD^{•-}. Our molecular movies**
50 **demonstrate how the protein environment of redox cofactors organizes multiple**
51 **electron/proton transfer events in an ordered fashion, which could be applicable to other**
52 **redox systems such as photosynthesis.**

53



54

55

56 All biological systems depend on electron transport chains (ETCs) to fuel their metabolism,
57 most commonly in the form of photosynthesis and respiration^{1,2}. Although ETC proteins, such
58 as cytochromes and iron-sulphur proteins³, can only transfer single electrons, ETC catalyzed
59 reaction cycles always result in the net flow of two electrons from donor to acceptor⁴. This
60 apparent paradox is solved by quinoid molecules such as membrane-resident quinones used by
61 photosynthetic reaction centres and respiratory chains as substrates or enzyme-bound flavin
62 adenine dinucleotide (FAD) and flavin mononucleotide (FMN) cofactors⁵. These molecules
63 can capture either one or two electrons and exist hence in three possible redox states: oxidized
64 (quinone), radical semi-reduced (semiquinone) or fully reduced (hydroquinone)⁶. One
65 particularly interesting example for multiple electron transfer (ET) reactions on FAD is the
66 [photoreduction](#) of DNA photolyases, a process by which this ubiquitous class of DNA repair
67 flavoenzymes reduces their FAD coenzyme to the catalytically active FADH⁻ state⁷. Here, two
68 light-driven, sub-nanosecond, single ET events transform inactive FAD_{ox} into the hydroquinoid
69 FADH⁻ via two long-lived radical semiquinone intermediates, FAD^{•-} and its subsequently
70 protonated form FADH^{•-} (Fig. 1a)⁸. The ETC fuelling these reactions consists mostly of a
71 tryptophan triad (Fig 1b)^{9,10}, or less frequently a tetrad¹¹, which ultimately extracts an electron
72 from the environment¹². In the photoactivated state, DNA photolyases finally catalyse blue
73 light-driven DNA repair of UV photolesions such as cyclobutane pyrimidine dimers (CPD)¹³
74 (Fig. 1c) by injecting an electron from excited FADH^{-*} onto the DNA lesion and transient
75 formation of semi-reduced FADH^{•-}¹⁴.

76 Over the last three decades, the flavin redox chemistry of photolyases has been extensively
77 characterized via spectroscopic and theoretical studies at ps-ns (reduction) and μs-ms (re-
78 oxidation) time-scales^{10,12,15-19}. However, information on the stabilization of the post-electron
79 transfer flavin species (ns-μs) by their surrounding protein matrix, which has been
80 hypothesized to enable quinoid chemistry^{8,20}, is lacking. Furthermore, spectroscopic

81 characterization was mostly restricted to electronic transitions of the flavin species and the ETC,
82 providing very little information regarding flavin geometry and thereby induced protein
83 conformational changes^{8,10,12,16,21}. In addition, flavin radical intermediates are too short-lived
84 for conventional crystallographic analysis, and the structures of flavoenzymes often suffer from
85 radiation-damage due to X-ray mediated flavin reduction²²⁻²⁵. Conversely, the recent
86 development of X-ray free electron laser (XFEL) facilities in combination with serial
87 femtosecond crystallography (SFX) techniques²⁶ has allowed for damage-free data collection
88 of biologically relevant macromolecular structures^{27,28}, particularly under time-resolved
89 conditions (TR-SFX) at ultrashort intervals^{22,29-36}.

90 In this study, we structurally characterize FAD redox- and post-electron transfer changes
91 in the nanosecond to millisecond range, and analyze how each intermediate species is stabilized,
92 as they occur in the *Methanosarcina mazei* class II DNA photolyase (*MmCPDII*)²³ via TR-
93 SFX. By analyzing a total of 23 structures, we were able to determine the redox- and time-
94 dependent structural changes in the FAD coenzyme elicited by the sub-nanosecond
95 photoreduction events, elucidate the mechanism of FAD^{•-} protonation, and uncover an FAD
96 redox sensor triad Asn/Arg-Asp that differentially stabilizes each flavin redox species, thus
97 providing unprecedented insight into the structural mechanics of quinoid-protein chemistry.

98

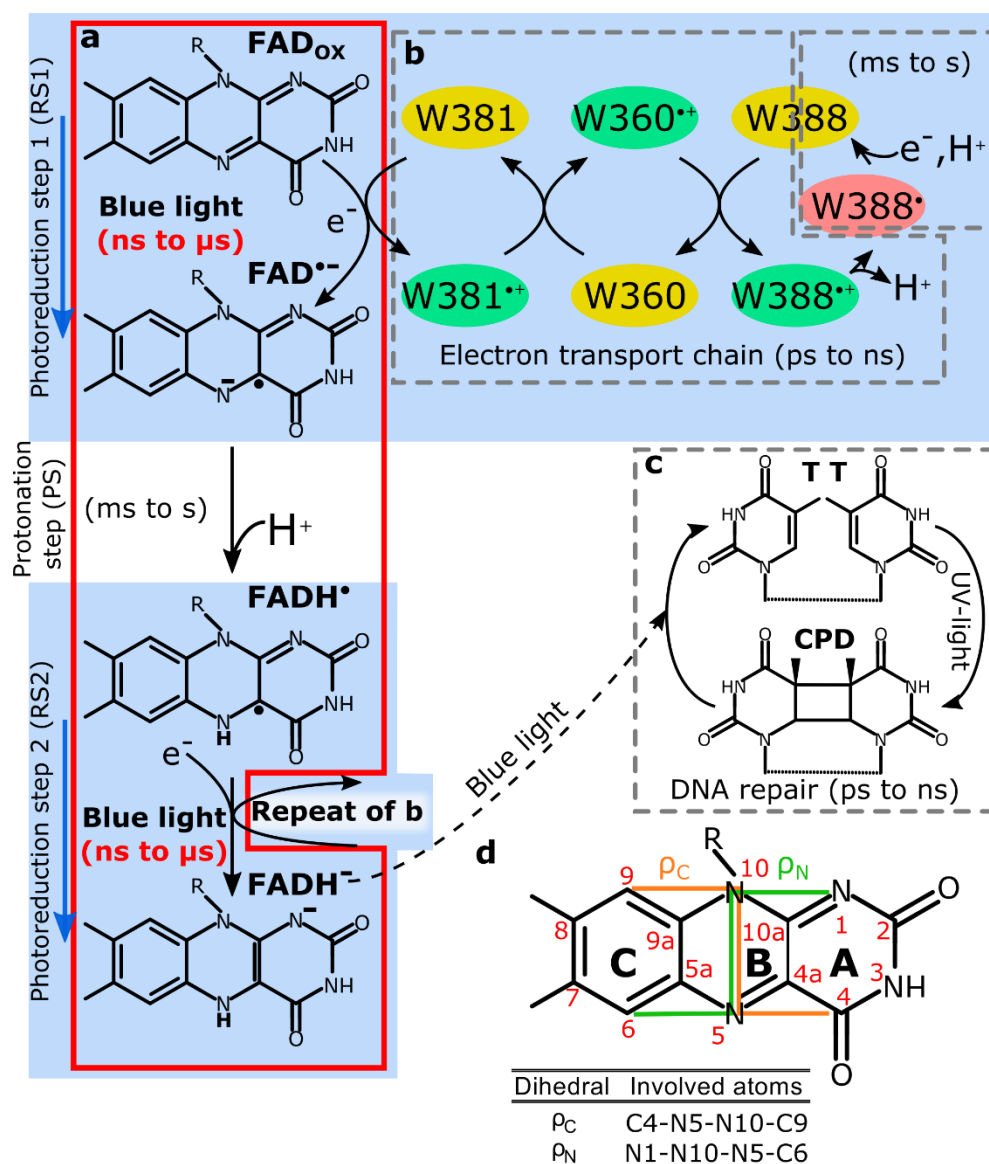


Figure 1. Reactions catalyzed by DNA photolyases. (a) During photoactivation, two photoreduction steps (RS1 and RS2, shaded blue) sequentially inject one electron each into FAD, reducing FAD_{ox} to FADH[•]. (b) Each photoreduction step involves a tryptophan triad (W381-W360-W388 in *Mm*CPDII), which acts as an electron transport chain. (c) Light-triggered repair of UV-damaged DNA containing a CPD. The time ranges marked in red in (a) were determined in this study, while all other timings are adapted from literature. (d) Isoalloxazine ring structure with definition of dihedral angles ρ_C (orange) and ρ_N (green).

100 **Results**

101

102 **Experimental approach and overall nomenclature**

103 In photolyases, and in the absence of an external reducing agent, photoreduction stalls at the
104 end of photoreduction step 1 (RS1), unable to proceed to photoreduction step 2 (RS2) without
105 prior protonation of the anionic semiquinone $\text{FAD}^{\cdot-}$ to the neutral semiquinone FADH^{\cdot} ^{9,10}. On
106 the other hand, the neutral semiquinone FADH^{\cdot} state is meta-stable at room temperature under
107 aerobic conditions²². Accordingly, static, or steady-state, datasets for the substrates and
108 products of both electron transfer reactions, i.e. oxidized, neutral semiquinone, and fully
109 reduced states, could be produced via controlled exposure to light and/or reducing agents
110 followed by data collection without illumination. Notably the unstable anionic semiquinone
111 state was an exception, as it could only be obtained via TR-SFX. Meanwhile, the TR-SFX
112 experiments of the two photoreduction steps could be performed separately, leading to 23
113 structures (Str1-Str23 in Tables 1 and S1-S3, and Figs. S1 and S2). Each structure is designated
114 as $E_{X/Y}$, with subscript X referring to the initial redox status (ox for oxidized, FAD_{ox} ; semi for
115 semiquinone, FADH^{\cdot} ; and red for reduced, FADH^-), and subscript Y describing their data
116 collection mode (“ss” for steady state, “dark” for a non-illuminated TR control structure, and
117 time for the delay after illumination). Furthermore, difference electron density maps³⁷ were
118 constructed to highlight structural differences, which are designated as the difference between
119 two states, $E_{X'/Y'} - E_{X/Y}$.

120 To monitor structural changes of the FAD isoalloxazine moiety, we introduce the ρ_C and
121 ρ_N dihedral angles (Fig. 1d). These changes happening upon FAD reduction were so far called
122 butterfly bending and defined as the angle (α) between the normal vectors of the A and C ring
123 planes (Fig. 1d)³⁸. Values close to zero degrees were derived for the oxidized flavin state, and
124 values of 15°-25° for the reduced hydroquinoid state of several flavoproteins³⁹⁻⁴¹. However, α

125 cannot discriminate between longitudinal twisting (bending along the long axis crossing the A,
126 B and C rings) and lateral bending or butterfly-like “buckling” (bending along the short *N5-*
127 *N10* axis)³⁸, whereas ρ_C and ρ_N can. When buckling dominates, $\rho_C \approx \rho_N \approx \alpha$; conversely, $\rho_C \neq \rho_N$
128 indicates a twist of the isoalloxazine moiety.
129

131 **Table 1.** Primary properties of the *Mm*CPDII TR-SFX structures.

Str. no.	Str. name	redox state	ρ_C angle	ρ_N angle	distance FADN5-R378N ϵ (Å) ^b	distance FADN5-N403O δ (Å) ^c	PDB code	resolution (Å) ^d
0 ^a	E _{ox/sync}	FAD _{ox}	7.6°	8.7°			7F8T ^e	1.50
1	E _{ox/ss}	FAD _{ox}	2.0°	2.0°	4.8	3.3	6LT3	2.25
<i>First time-resolved series (FAD_{ox} → FAD[•])</i>								
2	E _{ox/dark}	FAD _{ox}	2.0°	2.0°	4.8	3.4	6LM4	2.0
3	E _{ox/10ns}	FAD [•]	-3.6°	0.8°	4.7	3.6	6LMB	2.55
4	E _{ox/50ns}	FAD [•]	3.7°	6.6°	4.6	3.6	6LM5	2.25
5	E _{ox/250ns}	FAD [•]	17.1°	11.1°	4.6	3.7	6LM6	2.4
6	E _{ox/1μs}	FAD [•]	9.5°	13.4°	3.4	4.0	6LM7	2.2
7	E _{ox/10μs}	FAD [•]	30.9°	14.4°	3.2	3.7	6LM8	2.25
8	E _{ox/125μs}	FAD [•]	20.3°	18.8°	3.4	4.2	6LMC	3.0
9	E _{ox/400μs}	FAD _{ox} /FAD [•]	5.6°	4.8°	4.5	3.4	6LM9	2.4
10	E _{ox/1ms}	FAD _{ox}	4.4°	3.1°	4.5	3.4	6LME	3.0
11	E _{ox/5ms}	FAD _{ox}	3.3°	4.5°	4.8	3.4	6LMA	1.9
<i>Protonation step (FAD[•] → FADH[•])</i>								
12	E _{semi/ss}	FADH [•]	4.6°	4.75°	3.9	2.7	6LT1	2.1
<i>Second time-resolved series (FADH[•] → FADH[•])</i>								
13	E _{semi/dark}	FADH [•]	5.3°	4.7°	3.9	2.7	7CLW	2.10
14	E _{semi/10ns}	FADH [•]	9.7°	8.8°	4	2.5	7C3P	2.15
15	E _{semi/30ns}	FADH [•]	11.3°	11.5°	3.6	2.7	7C3R	2.1
16	E _{semi/100ns}	FADH [•]	11.3°	9.6°	3.7	2.8	7C3W	2.3
17	E _{semi/300ns}	FADH [•]	16.5°	16.8°	3.4	2.7	7C3X	2.5
18	E _{semi/1μs}	FADH [•]	9.7°	9.7°	3.6	2.6	7CLM	2.1
19	E _{semi/5μs}	FADH [•]	12.7°	11.5°	3.7	2.8	7CLN	2.1
20	E _{semi/10μs}	FADH [•]	8.5°	8.5°	3.9	2.6	7CLO	2.1
21	E _{semi/30μs}	FADH [•]	10.9°	10.6°	3.8	2.7	7CLP	2.1
22	E _{semi/100μs}	FADH [•] /FADH [•]	5.3°	5.5°	3.9	2.6	7CLQ	2.15
<i>Full reduction at steady state</i>								
23	E _{red/ss}	FADH [•]	14.3°	14.5°	3.3	3.1	6LT2	2.20

132 ^aPreviously reported structure from synchrotron X-ray data²³. The dihedral angles were not reported,
133 and were obtained from refining by our procedures.

134 ^bThe FADN5-R378N ϵ distance is between the FAD isoalloxazine N5 atom and the Arg378 N ϵ atom.

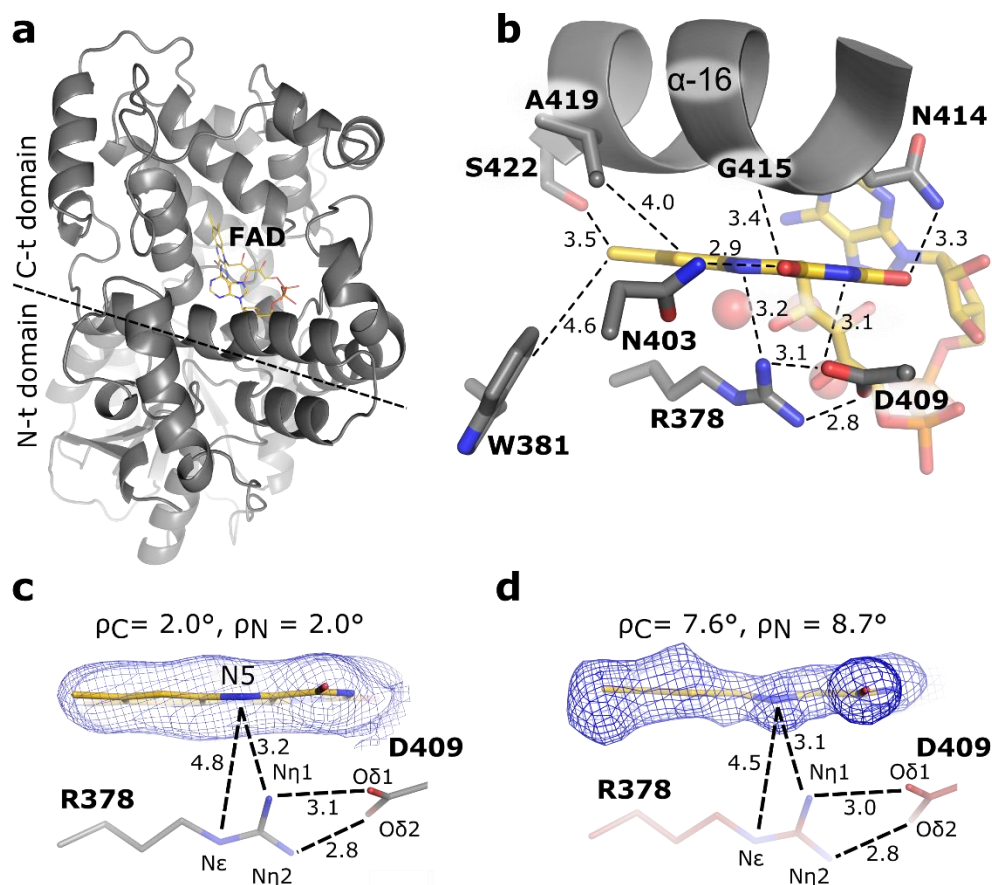
135 ^cThe FADN5-N403O δ distance is between the FAD isoalloxazine N5 atom and the Asn403 O δ 1 atom.

136 ^dResolution values given here correspond to the extrapolated structure factor dataset.

137 ^eThis structure is derived from 2XRY with dihedral angles refined by the approach of this work.

139 **The damage-free structure of oxidized *Mm*CPDII**

140 Like the structure of $E_{\text{ox/sync}}$, previously solved by conventional synchrotron X-ray
141 crystallography¹⁰ (Str0 in Table 1), our steady-state oxidized structure $E_{\text{ox/ss}}$ (Str1), solved at
142 room temperature by SFX, consists of a two-domain topology (Fig. 2a), with the isoalloxazine-
143 interacting elements being the hydrophobic side of helix $\alpha 16$ and sidechains of Asn403, Arg378,
144 and Asp409 (Fig. 2b). However, the isoalloxazine ring of our $E_{\text{ox/ss}}$ is only slightly buckled
145 with ρ_C , ρ_N dihedrals of 2.0° and 2.1° (Fig. 2c), substantially smaller than that of 7.6° and 8.7°
146 for the synchrotron structure $E_{\text{ox/sync}}$ as processed by our approach [for comparison with TR-](#)
147 [SFX structures](#) (Fig. 2d). The difference can be attributed to $E_{\text{ox/ss}}$ being the purely oxidized
148 form as characterized by *in crystallo* UV-Vis [absorption](#) spectra (Fig. S3a), whereas $E_{\text{ox/sync}}$ has
149 been partially reduced by synchrotron X-ray irradiation as supported by *in crystallo* spectra²³.
150 In addition, as shown in Table 1, the $E_{\text{ox/dark}}$ structure (Str2, time zero) is nearly identical to the
151 steady-state $E_{\text{ox/ss}}$ structure, providing validation for the TR-SFX experiments.



152

Figure 2. Structure of oxidized *Mm*CPDII photolyase. (a) Global structure of E_{ox/ss} (Str1, steady state oxidized) showing the overall fold with FAD depicted in gold. (b) Isoalloxazine binding pocket with interacting residues (grey sticks) and waters (red spheres). None of the waters are within the hydrogen bonding distance to N5. (c) Geometry of the E_{ox/ss} FAD isoalloxazine ring showing minor buckling. (d) Geometry of the isoalloxazine ring from the synchrotron X-ray structure E_{ox/sync} (Str0)²³ after reprocessing with our approach, showing increased buckling angles due to radiation-induced photoreduction. In c-d, SigmaA-weighted $2mF_{\text{obs}} - DF_{\text{calc}}$ omit maps surrounding the isoalloxazine moiety (blue mesh, 1σ contour level) are shown.

153

154 **Changes in active site structures following ET**

155 In both photoreduction steps, structural changes of the isoalloxazine ring and its surrounding
 156 residues occur after ET, from the first time-point at 10 ns up to roughly 1-10 μs. Detailed
 157 analyses indicate that these structural changes involve mainly the geometry of the isoalloxazine
 158 ring, the Arg378-Asp409 salt bridge underneath it, and the sidechain of Asn403 close to the

159 isoalloxazine N5 atom, which are summarized in Table 1. The time courses of the changes in
160 structural parameters from Table 1 are plotted in Figure 3a,c (RS1) and b,d (RS2), while
161 representative structures and difference density maps are shown in Figure 3e,h (RS1), g,j (RS2),
162 and f,i (the protonation step, PS), which will be addressed in subsequent sections.

163 On the other hand, the ETC tryptophans (Fig. 1b) are not a subject of this study as there
164 are no significant structural changes in either of our time-resolved series (Fig. S4a,b), in
165 agreement with previous spectroscopic studies indicating that, for *Mm*CPDII, the initial light-
166 driven electron transfer completes in less than a nanosecond¹⁰. Interestingly, we did observe
167 conformational changes of a few residues (H343, H356, and N361) surrounding Trp388 around
168 the first time-point of 10 ns (Fig. S4c,d), supporting that electron transfer and structural changes
169 in a redox reaction can be dissected by TR-SFX.

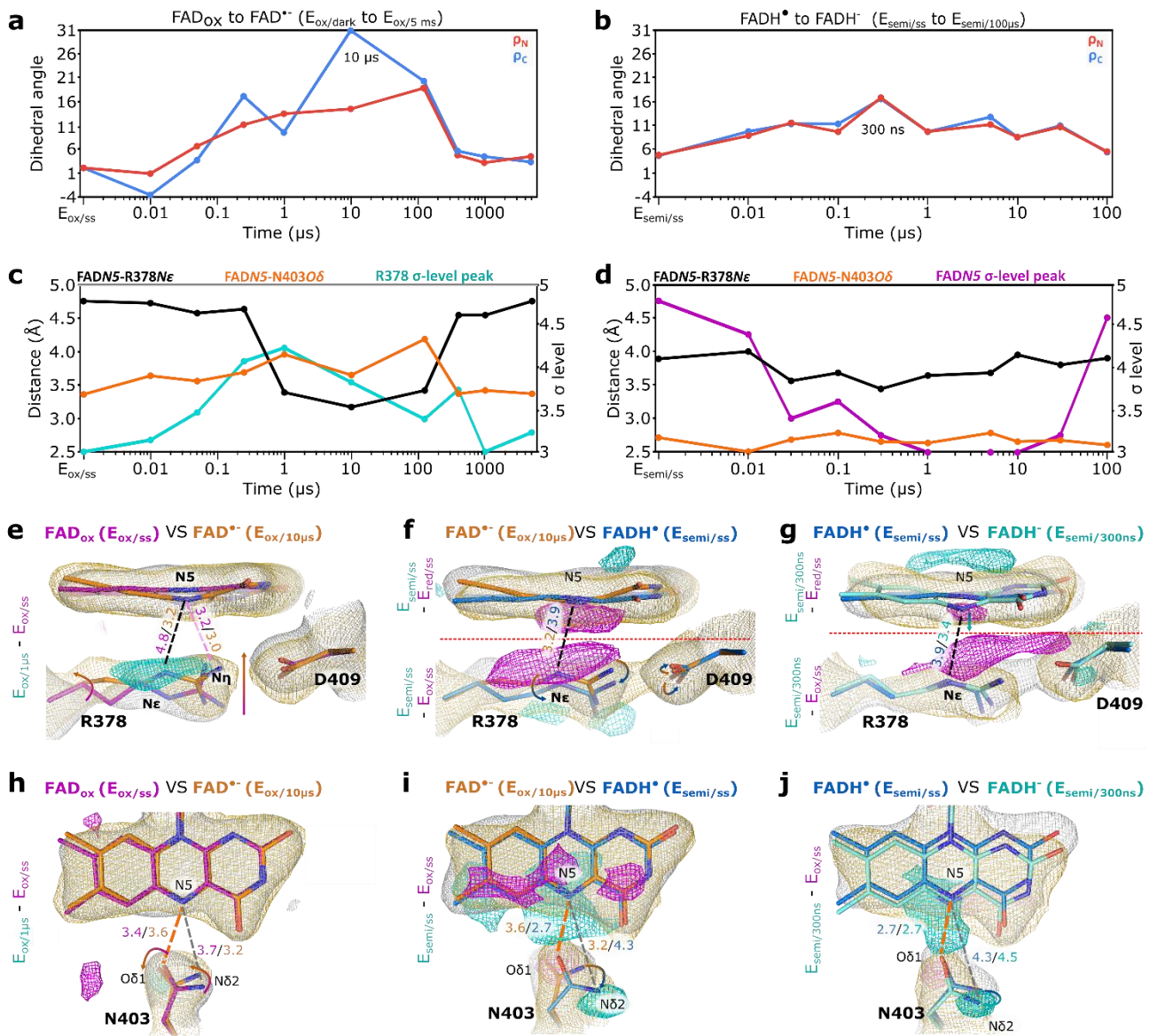
170

171 **Changes in the isoalloxazine geometry**

172 During RS1, the FAD_{ox} to FAD[•] transition (Fig. 3a), ρ_C values change from 10 ns, reaching a
173 maximum at 10 μ s, whereas ρ_N values follow the same pattern but with milder changes,
174 suggesting a twist. On the other hand, from 125 μ s after photoexcitation, ρ_C and ρ_N have both
175 decreased substantially, and by 400 μ s have returned to their initial values, correlating well
176 with the reversion of structural changes in the vicinity Trp388 (Fig. S4c,d). This apparently
177 reflects FAD[•] reoxidation via back electron transfer toward Trp388[•] (Fig. 1a, b), as under our
178 experimental conditions the transiently formed tryptophan radical is present due to the lack of
179 external reductants^{9,10}. As indicated by kinetic data¹⁰, the estimated half-life of FAD[•] is less
180 than a millisecond (Fig. S3b).

181 During RS2 (FADH[•] to FADH⁻, Fig. 3b), the ρ_C and ρ_N dihedral angles increase together
182 with time and reach a maximum at 300 ns (16.5° and 16.8°, respectively, Table 1), correlating
183 fairly well with the values in the fully reduced steady-state E_{red/ss} (14.3°, 14.5°, respectively).

184 However, they are both reverted to $\sim 7^\circ$ by 100 μs , again indicating the onset of reoxidation of
185 the isoalloxazine ring. Accordingly, difference maps relative to $E_{\text{red/ss}}$ (Fig. 3g and Fig. S2a)
186 show a negative density peak below the central ring B of the isoalloxazine, which decreases to
187 the noise level (3σ) past 300 ns and increases again past 10 μs (Fig. 3d, magenta curve).
188 Importantly, observation of the parameters reaching a peak and relaxing back in Figure 3a-d
189 provides further support that the observed small changes are significant and mirror reversible
190 redox-dependent changes. In summary, the time-resolved structural analysis of both
191 photoreduction steps illustrates how, after initial ET, the isoalloxazine moiety re-hybridizes to
192 its new redox state and reaches its final structure in about one **to ten** microseconds. Our results
193 above expand the description of a redox reaction of FAD to include subsequent structural
194 changes in addition to the ET steps.



195

196 **Figure 3. Structural changes during the photoactivation of *Mm*CPDII.** (a,b) Evolution of ρ_C (blue)

197 and ρ_N (red) dihedral angles over time for photoreductions 1 and 2, respectively. (c,d) Evolution over

198 time of the FADN5-R378Nε (black curve) and FADN5-N403Oδ distances (orange curve), along with

199 plots of the σ -levels of the positive difference peak near R378Nε (c, cyan curve) and the negative

200 difference peak below FADN5 (d, magenta curve). (e-g) Structures of the isoalloxazine ring and the

201 nearby Arg378-Asp409 salt bridge at the beginning and end of each photoreduction step. For RS1 (e),

202 E_{ox/ss} (FAD_{ox}) is superposed with E_{ox/10μs} (FAD[•]), for PS (f), E_{ox/10μs} (FAD[•]) with E_{semi/ss} (FADH[•]), and

203 for RS2 (g), E_{semi/ss} (FADH[•]) with E_{semi/300ns} (FADH⁻). Each panel is also superposed with **2σ contoured**

204 **2DFo-mFc omit maps** corresponding to the beginning (grey) and end (gold) states of each

205 **photoreduction step, as well as** difference maps as indicated by the vertical labels left to the structural

206 moiety. Difference map contour levels: (e) 3σ, (f-g) 3.5σ near the isoalloxazine moiety (above the red

207 dotted line) and 4.0σ near the salt bridge (below the red dotted line). (h-j) Redox- and time-dependent

208 FAD N5-Asn403 interaction for the same structures as in e-g, respectively. **Omit maps as above, as well**

209 as difference maps relative to $E_{ox/ss}$ (4σ) are also shown. In all structures, arrows indicate motion, while
210 dotted lines the FAD $N5$ -R378 $N\epsilon$ (black) and FAD $N5$ -N403 $O\delta$ (orange) distances in Å. In all difference
211 density maps, cyan indicates positive and magenta indicates negative.

212

213 **Conformational changes of Arg378 concurrent with bending of FAD isoalloxazine ring**

214 For RS1, a positive peak (from difference maps relative to $E_{ox/ss}$) appears above Arg378 $N\epsilon$
215 (Fig. 3e and Fig. S1a). When its σ -level is plotted against time (cyan curve in Fig. 3c), it reveals
216 a progressive change peaking at 250 ns to 10 μ s, followed by a back relaxation till 1-5 ms,
217 suggesting a movement of Arg378 $N\epsilon$ toward the $N5$ atom of FAD concurrent with bending
218 and subsequent relaxation of the isoalloxazine ring. In agreement, the FAD $N5$ -R378 $N\epsilon$
219 distance (Table 1) decreases and then reverts back following the same pattern (Fig. 3c, black
220 curve). Importantly, structural analyses indicate that while Arg378 $N\epsilon$ moves toward FAD $N5$,
221 the bifurcated Arg378-Asp409 salt bridge remains in place (Fig. 3e and Fig. S1a).

222 The same correlation between the FAD $N5$ -R378 $N\epsilon$ distance and isoalloxazine bending
223 was also observed in RS 2 (FADH^{*} to FADH⁻). As shown by the black curve in Figure 3d, the
224 distance becomes progressively shorter, reaching a minimum at 300 ns where isoalloxazine
225 bending is most pronounced (Fig. 3b), and again relaxes back to the starting point at 100 μ s.
226 However, the change in the FAD $N5$ -R378 $N\epsilon$ distance in the second set is smaller than that in
227 the first set (black curves in Fig. 3c,d). Accordingly, the closing between FAD $N5$ and R378
228 $N\epsilon$ in the second set is likely caused mainly by the out-of-plane movement of FAD $N5$. In
229 support, the Arg378 sidechain remained unmoved during RS2 as explained below. Meanwhile,
230 the structural changes and the two different mechanisms described above for the two TR-SFX
231 series and additional results below can be visualized in Videos S1 and S2.

232

233 **Protonation of FAD⁻ and weakening of the Arg378-Asp409 salt bridge**

234 Protonation of FAD^{•-} at the *N5* position is essential for the photoactivation, as only the neutral
235 semiquinone FADH^{•-} can be further reduced to the active FADH⁻ state (Fig. 1a). However, the
236 proton donor and molecular mechanism remain elusive⁴². Our structural data points toward a
237 close involvement of the Arg378-Asp409 salt bridge in this step, as its geometry is strongly
238 affected by the FAD^{•-} protonation. As shown in Figure 3f, the Arg378 guanidinium moiety
239 moves away from the isoalloxazine ring after the FAD^{•-} to FADH^{•-} conversion, reverting to a
240 similar position to the oxidized state. However, the geometry of the bifurcated salt bridge is
241 altered by this FAD^{•-} to FADH^{•-} conversion, causing Arg378 sidechain to break its salt bridge
242 with Asp409 with a swivelling motion (Fig. 3f). In support, difference maps from the second
243 series, relative to E_{ox/ss}, reveal a very clear negative signal above the Arg378 sidechain (Fig. 3g
244 and Fig. S2b), in contrast to the positive difference peaks in the first photoreduction step (Fig.
245 3e and Fig. S1a). Meanwhile, no significant peaks were observed relative to the fully reduced
246 state E_{red/ss} (Fig. S2a). Furthermore, the intensity of the above mentioned negative difference
247 map peak remained approximately constant (Fig. S2b), and additional difference map peaks
248 surrounding guanidinium-carboxylate appeared (Fig. 3f-g).

249 These results, along with absence of other efficient proton donors or water molecules
250 within hydrogen bonding distance to the isoalloxazine *N5* nitrogen (Fig. 2b), suggest that
251 Arg378 is likely the proton donor for the protonation of FAD^{•-} to FADH^{•-}. In support, the
252 Arg378-Asp409 ionic pair is highly conserved, as database analysis of all known photolyase-
253 cryptochrome family (PCF) sequences (19524) showed that only three class II photolyases and
254 six cryptochromes lack this Arg-Asp salt-bridge. Our attempt to construct these unusual natural
255 mutants resulted in either protein aggregation or loss of FAD binding (Tables S4-S5). Only the
256 conservative R378K mutation yielded a well-behaved, monodisperse protein capable of FAD
257 uptake, but at only ~20% stoichiometry (Fig. S5a) and with non-specific binding (Fig. S5b).

258 These results explain why a key function for this highly conserved pair⁴³⁻⁴⁵ has never been
259 reported before for any member of the PCF.

260

261 **Facilitation of protonation and stabilization of the protonated state by Asn403**

262 The *N5* nitrogen of free FADH[•] has been shown to be a weak acid (pK_a 8.5)⁴², which is
263 insufficient for its conjugate base FAD^{•-} to drive proton transfer from Arg378 (pK_a ~12.5).
264 However, a previous report showed that the pK_a of the *N5* nitrogen of flavodoxin's
265 semiquinone FMNH[•] coenzyme is raised to >13 due to an H-bond with a backbone carbonyl
266 oxygen⁴⁵. A similar interaction between isoalloxazine *N5* of FADH[•] and the equivalent of
267 *MmCPDII* Asn403 *OδI* atom has been reported by FT-IR studies of other photolyases^{43,44}, a
268 behavior we can now explain with our structures: In FAD_{ox}, Asn403 *OδI* is closer to FAD_{ox}
269 *N5*, while *Nδ2* mainly interacts with the carbonylic FAD_{ox} *C4=O*. During RS1, photoreduction
270 to FAD^{•-} causes the Asn403 amide sidechain to rotate, with *OδI* moving away from *N5*, while
271 *Nδ2* approaching it (Fig. 3h). Upon protonation to FADH[•] (Fig. 3i), the Asn403 sidechain
272 swivels, bringing the Asn403 *OδI* atom in close proximity to the *N5*-H, whereas *Nδ2* moves
273 to a distal position, which nevertheless allows it to continue interacting with *C4=O* (Fig. S2c).
274 In accordance with FT-IR data, the FADH[•] state structure (Fig. 3j) is somewhat in-between, as
275 the Asn403 swivel is partially maintained. Although previous mutagenesis studies of Asn403
276 in *MmCPDII* suggested an important role in photoreduction²³, our results provide structural
277 evidence for stabilization of the protonated state by H-bonding between isoalloxazine *N5* and
278 Asn403 *OδI*, and support an unusually high pK_a for the FADH[•] *N5* position in photolyase.

279 Furthermore, the comparison between the FAD isoalloxazine *N5* to Asn403 *OδI* distance
280 (FAD_{N5}-N403*Oδ* distance, orange curves in Fig. 3c-d) and the FAD_{N5}-R378*Nε* distance
281 (black curves in Fig. 3c-d) shows an inverse relationship in both TR sets. Together, the results
282 suggest that, during RS1, Arg378 approaches the FAD^{•-} isoalloxazine *N5* but Asn403 *OδI*

283 recedes away. During PS, Arg378 moves away whereas Asn403 *Oδ1* moves in to form an H-
284 bond with the isoalloxazine *N5*-H. Then, upon RS2, isoalloxazine *N5* moves again toward
285 Arg378 due to enhanced buckling, leading to slight lengthening of the H-bond with Asn403
286 *Oδ1*. As shown in Table 1 and Figure S2b, the $E_{\text{semi}/300\text{ns}}$ structure is strikingly similar to the
287 steady-state reduced structure $E_{\text{red/ss}}$. These results indicate intricate coordination between
288 Arg378 and Asn403 to mediate the two photoreduction and protonation steps and stabilize the
289 intermediate species in the process.

290

291 **The FAD redox sensor triad and the overall mechanism of photoactivation**

292 Our data shows how Asn403, Arg378 and Asp409 function closely as an “FAD redox sensor
293 triad” to mediate structural changes of the FAD isoalloxazine, from ns to μs after the initial
294 electron transfer in both photoreduction steps and the in-between protonation step. The
295 structural changes are small (Fig. 4a), but they have been exquisitely dissected by a large
296 number of TR-SFX structures with continuous changes and intricate coordination involving an
297 extensive H-bonding network (Fig. 4b). While Figure 3a-d show complete forward reaction
298 and back relaxation for each photoreduction step separately, here we merge the two forward
299 reactions and address the overall mechanism in four ways: H-bond analysis to show the
300 variation of each H-bond in each intermediate structure (Fig. 4c), structural schematics based
301 on the results of individual steps (Fig. 4d), merging of dihedral angles and interatomic distances
302 from Figure 3 (Fig. 4e), and visual illustration (Video S3). These analyses together are
303 explained below.

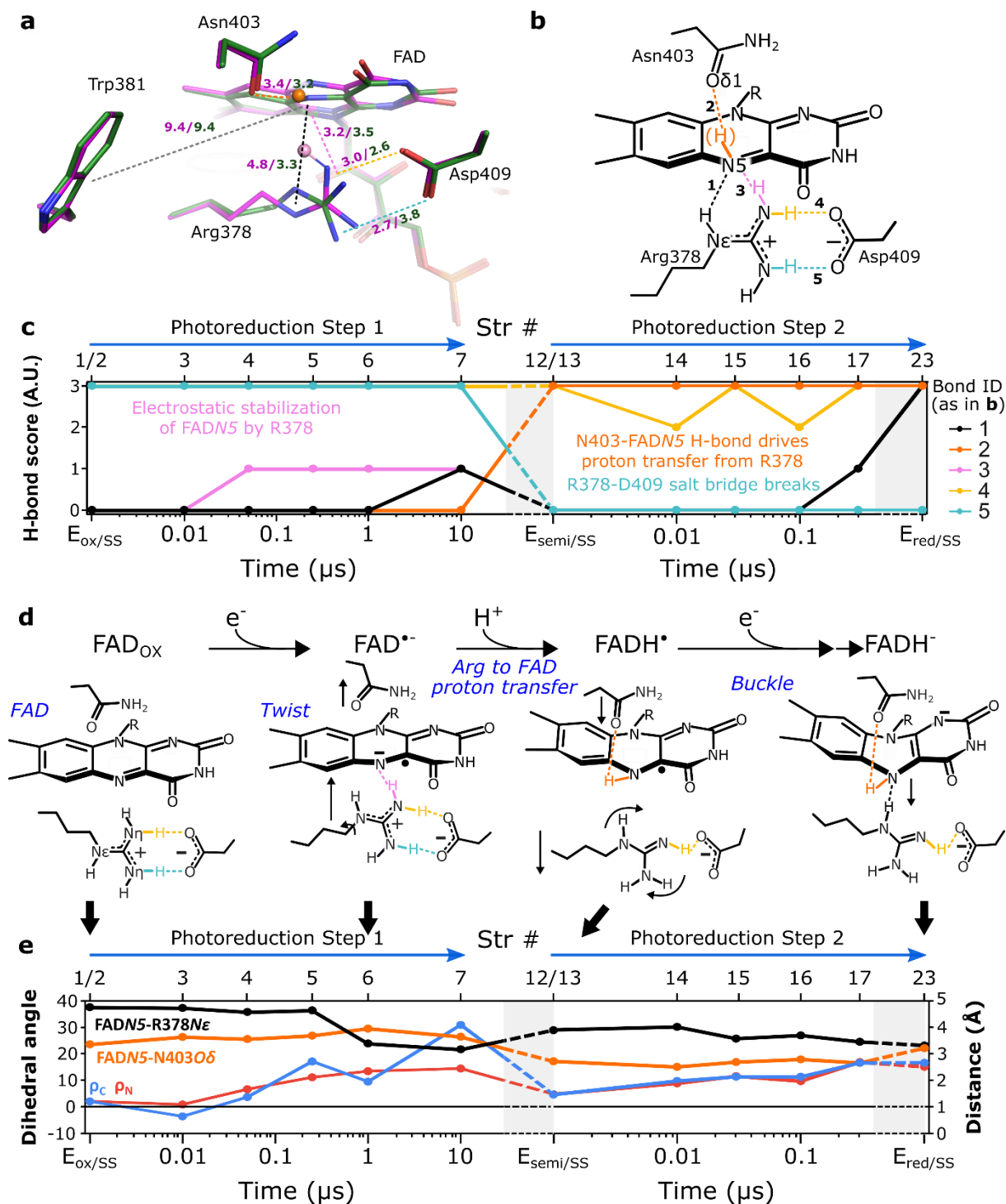
304 In RS1, i.e. the transition from FAD_{ox} to FAD^* , a negative charge builds up at FAD *N5*,
305 electrostatically repulsing the Asn403 *Oδ1* atom and attracting both Asn403 *Nδ2* and, more
306 importantly, the positive Arg378 sidechain in preparation for protonation. The result is a
307 transient H-bond between the proximal Arg378 *Nη* and FAD *N5* (Figs. 3e, 4c-d). Accordingly,

308 between 1 μ s and 125 μ s (FAD^{•-}), the FADN5-R378N ϵ distance is the shortest (i.e. the most
309 stabilized isoalloxazine moiety), whereas the FADN5-N403O δ distance is the longest (i.e. the
310 least degree of destabilization) (Figs. 3c, 4e).

311 When the sidechain of Arg378 is close enough to FAD N5, proton transfer occurs. FADH[•]
312 and Arg378, now both neutral, interact only weakly with each other, with Arg378 receding
313 from the isoalloxazine moiety and the Asp409 sidechain (Fig. 3f). Instead of behaving as an
314 ionic pair, the Arg378 and Asp409 are now connected by a single H-bond (Fig. 4c-d). A driving
315 force for the FAD N5 protonation is its interaction with Asn403 O δ 1, which moves in to form
316 an H-bond, becoming the main stabilizing element for the neutral semiquinone state (Fig. 3i,
317 E_{semi/ss}, FADN5-N403O δ distance 2.7 Å).

318 Then, in RS2, the same trends are observed, with Asn403 O δ 1 moving slightly away but
319 still maintaining the hydrogen bond, while isoalloxazine buckling closes the gap to Arg378 N ϵ ,
320 reaching maximal changes at 300 ns to 1 μ s (Figs. 3d, 3g, 4c-e) and resulting in a very close
321 approximation of the steady-state E_{red/ss}, which represents the fully reduced FADH⁻ state, and
322 where both FADN5-N403O δ and FADN5-R378N ϵ H-bonds contribute to the stabilization of
323 FADH⁻.

324



325

326 **Figure 4. Mechanistic view of *MmCPDII* photoactivation.** (a) Superposed active site structures of
 327 *MmCPDII* in the oxidized (purple) and reduced (green) states. The pink ball-and-stick model designates
 328 the proposed Arg378 proton to be transferred to FAD N5, the orange after transfer. Distances of interest
 329 are color coded as dashed lines, with the black one corresponding to the FADN5-R378N ϵ distance,
 330 while the orange one the FADN5-N403O δ distance. (b) Schematic representation of key elements in
 331 the Asn403-isoalloxazine-Arg378-Asp409 H-bonding network. Bonds of interest are labeled by a
 332 number and a color. (c) Plots summarizing the dynamic behavior of the H-bonding network. Line colors

333 on the graph follow those in (b). H-bond scores are based on a previous PDB-wide analysis and
334 described in Methods. Briefly, a score of 1 indicates three necessary conditions have been met, while
335 2, 3 indicate additional favorable conditions. The top axis indicates structure numbers from Table 1. (d)
336 Structural schematics of the redox and protonation reactions. Only the relevant hydrogen bonds for each
337 state are shown, color coded as in b and c. (e) Merging of the dihedral angles and distance plots from
338 Figure 3a-d, showing continuous changes in the entire photoactivation process (i.e., by excluding the
339 back relaxation time points). In both c and e, a grey background indicates reaction steps whose timing
340 is not well defined by our experiments.

341

342 **Discussion**

343 Overall, this work describes the first structural description of the microscopic processes of the
344 [photoreduction](#) of a DNA photolyase, highlighting geometric changes of the isoalloxazine
345 moiety in the re-hybridization process, how they are mediated by Asn403/Arg378-Asp409,
346 which we name a redox sensor triad, and enable a typical quinone chemistry, namely sequential
347 pumping of two electrons separated by a protonation step. The X-ray damage-free structure of
348 *Mm*CPDII shows that the catalytically active FADH⁻ chromophore adopts a bending angle of
349 about 14°, and that bending of the FADH⁻ isoalloxazine delicately controls the ET potential by
350 affecting forward as well as backward electron transfers. Although the observed bending in the
351 photolyase is well below the degree of bending of FADH⁻ in free solution (24°-33°)⁴⁶, it is
352 significant for the DNA repair mechanism of photolyases as most previous theoretical
353 calculations on ET reactions between the isoalloxazine and the CPD and (6-4) DNA lesions
354 predicted planarity of the isoalloxazine due to a lack of interaction with the protein matrix in
355 QM models⁴⁷. Planarity was also postulated from the photochemistry of catalytically
356 competent photolyases in the FADH⁻ state⁸, because flexible butterfly motions across conical
357 sections would cause rapid deactivation of excited FADH^{-*} states rather than electron transfer
358 to the bound DNA lesion. Our structures of the FADH⁻ state show that these flexible motions
359 can be avoided by increased interaction with the arginine and asparagine of the redox triad,

360 thus leading to a higher rigidity of the flavin binding site and explaining the bathochromically
361 shifted and lifetime-elongated fluorescence emission spectra of FADH⁻ in photolyases when
362 compared to free solution⁸.

363 In terms of the photoreduction to FADH⁻, four features of its molecular mechanism are
364 fundamental for not only photolyases, but also other flavoenzymes. First, electron uptake in
365 small molecules in solution and in photolyases by FAD takes place at similar time-scales^{9,48}
366 with subsequent geometric changes requiring only picoseconds in the former⁴⁸. However, we
367 found that the equivalent response of the protein-embedded isoalloxazine moiety is delayed by
368 nanoseconds to microseconds. This can now be explained by the role of the protein matrix for
369 stabilizing otherwise highly unstable intermediates such as FAD^{•-} by allowing them to probe a
370 wide region of the conformational space via twisting and buckling. These transient structural
371 changes increase the probability of ulterior reactions, first triggering of proton transfer (PT) to
372 form FADH[•] and then further photoreduction to FADH⁻. This conclusion extends previous
373 theoretical studies, which proposed that buckling and twisting motions in the isoalloxazine ring
374 just serve for controlling the redox chemistry of flavins³⁸. We found that they can also actively
375 participate in PT pathways with the embedding protein matrix, thus highlighting the role of the
376 protein in controlling quinone chemistry.

377 Secondly, our data uncovered a redox sensor triad Asn/Arg-Asp. A structure-based PDB
378 wide survey in which we searched for flavoproteins presenting an Arg-Asp(Glu) pair nearby
379 their isoalloxazine moieties returned only PCF members, supporting the unique functional roles
380 of this conserved motif. Interestingly, within PCF, the third residue, asparagine, is conserved
381 in enzymatically active photolyases, but not in solely photosensory cryptochromes, where this
382 residue can be replaced by aspartate like in plant cryptochromes or cysteine in insect
383 cryptochromes⁴⁹. In those with alternative redox triads (Asp/Arg-Asp and Cys/Arg-Asp), the
384 quinone chemistry is significantly affected, with photoreduction leading to single electron

385 uptake and protonation to FADH[•] in the former⁵⁰, while the latter arrests photoreduction in the
386 FAD^{•-}⁵¹.

387 Thirdly, despite its high sidechain pKa, the function of arginine as a proton donor has been
388 suggested for several enzymes⁵²⁻⁵⁶. Our results provide structural intermediates before and
389 after protonation of isoalloxazine N5 by Arg378 in the *Mm*CPDII photolyase. Furthermore,
390 widening the above-mentioned PDB search for non-protein acidic ligands nearby an arginine
391 and a flavin revealed six flavin-dependent oxidoreductase families (Table S6) with specific
392 examples from each family shown in Figure S6, including the fumarate reductase mentioned
393 above⁵² and suggesting a potentially wide catalytic role for such an arrangement.

394 Finally, intramolecular ET reactions in photolyases were often understood as simplest
395 biological model systems for comparable processes during the light-driven charge separation
396 in photosynthetic reaction centres. The uptake of electrons and protons by quinone substrates
397 in the Q_B binding site is known to follow an ordered ET-PT-ET-PT scheme⁵, thus being
398 comparable to the ET-PT-ET scheme of photolyases, and is accompanied by a redox-dependent
399 move of Q_B from a distal to a proximal binding site. Notably, protonation of Q_B^{•-} as formed
400 after first ET is supposed to occur via a serine, Ser-L223 in bacterial reaction centres⁵⁷. Given
401 our unexpected finding that an arginine conserved in the PCF serves as proton donor to the
402 flavin cofactor, but not the other candidate asparagine of the redox triad, we expect that similar
403 time-resolved structural studies will be necessary in future to nail down PT events in other
404 complex biological redox systems, e.g. the photosynthetic reaction centres.

405

406 **Methods**

407 **Protein production, crystallization and preparation for XFEL**

408 Protein was produced, and crystals were obtained, by upscaling previously published
409 conditions²³. Concentrated crystal slurries were produced by centrifugation of crystallization
410 batches. For obtaining a fully oxidized dataset, the crystal slurry was then embedded in a
411 hydrophobic grease matrix in a 1:9 crystal:matrix ratio, as described elsewhere⁵⁸. After this
412 point, the sample was maintained under far red light (650 nm) at all times to avoid in-situ
413 photoreduction.

414 For obtaining the semiquinone crystalline material used to acquire the $E_{\text{semi/ss}}$, $E_{\text{semi/dark}}$
415 and all $E_{\text{semi/t}}$ structures (Table 1), the crystal slurry was first supplemented with 50 mM DTT.
416 For full reduction, the crystal slurry was then exposed to bright white light (Leica KD300) for
417 5 minutes, and then for partial oxidation to air for another 20 minutes, followed by embedding
418 in grease matrix. The production and handling of fully photoactivated *Mm*CPDII crystals ($E_{\text{red/ss}}$)
419 was analogous to semiquinone, but to avoid oxidation, the entire procedure was performed
420 under anaerobic conditions.

421

422 **Data collection.**

423 All 23 structures (Str1-Str23 in Tables 1 and S1-S3 and Figs. S1 and S2) were obtained at the
424 SPring-8 Angstrom Compact free electron LAser (SACLA)⁵⁹, with crystals being excited via
425 a nanosecond pulse from a 408 nm OPO laser running at 15 Hz, while data collection from
426 XFEL pulses at 30Hz.

427

428 **Data processing and structural solution**

429 All collected images were initially sorted on-site with cheetah⁶⁰, and then processed off-site
430 with CrystFEL 0.6.2⁶¹. Processed datasets were then scaled via SCALEIT, a piece of software
431 within the CCP4i crystallographic suite⁶². Molecular replacement structural solution was
432 performed for $E_{\text{ox/ss}}$ via Phaser, also part of CCP4i, using the [original](#) $E_{\text{ox/sync}}$ ²³ (PDB code
433 2XRY) as the search model. Further datasets were then solved based on $E_{\text{ox/ss}}$, or its derived
434 structures.

435

436 **Overall refinement and structural data visualization**

437 Structure factor extrapolation^{31,36,63} was used to refine the subtle time- and redox-dependent
438 structural changes (Fig. S1 and S2 for the two time-resolved series). Furthermore, difference

439 electron density maps³⁷ were constructed to highlight these structural differences, which are
440 designated as the difference between two states, $E_{X'/Y'}-E_{X/Y}$. Quantitative analysis of difference
441 map peaks was normalized to σ levels, i.e. the factor by which a peak's magnitude exceeds the
442 background electron density. Our results showed that significant difference maps were only
443 observed in the active site region as shown by examples in Figures S7 and S8. Meanwhile for
444 RS1, ultrafast conformational changes around 10 ns also occurred in the vicinity of Trp388,
445 the final electron donor in the electron transfer chain, in the absence of an external reducing
446 agent (Fig. S4c,d). Since RS2 was performed in the presence of reducing agent DTT, W388•
447 can be regenerated to W388 and the ultrafast conformational change could not be observed.

448

449 **Refinement of the FAD isoalloxazine moiety and its conformational changes**

450 To follow the bending of FAD in our structures, and avoid model bias, the dihedral angles for
451 all structures, as listed in Table 1, were calculated by adapting previous real space correlation
452 methods established for the analysis of TR-SFX data as it applies to subtle changes in
453 photoreceptor chromophores^{36,64,65}. Briefly, an equilibrium ensemble for the FAD redox
454 dependent conformational space was computationally generated based on the $E_{ox/ss}$, $E_{semi/ss}$ and
455 $E_{red/ss}$ datasets, from which minimum and maximum ρ_C and ρ_N values (Fig. 1d) could be
456 determined. Then, ρ_C and ρ_N restraints within those limits were applied stepwise to each dataset
457 via three cycles of Phenix refinement⁶⁶ using the corresponding resting structure as the initial
458 model (Fig. S9). The software sfall was then employed to produce calculated structure factors
459 from both the initial (F_{ci}) and refined (F_{cref}) models, and $F_{cref}-F_{ci}$ maps within 2.5 Å of the
460 isoalloxazine moiety were calculated using the initial model phases, analogously to the
461 experimental maps presented in e.g. Figure 3. Finally, in order to assess the quality of the
462 resulting isoalloxazine geometry, the real space correlation coefficient (CC) between the $F_{cref}-$
463 F_{ci} and the corresponding $F_{X'/Y'}-F_{X/Y}$ maps was calculated. Accordingly, we could produce
464 heat maps where ρ_C and ρ_N values were correlated to the CC, to the degree they were able to
465 reproduce the observed difference density features. A final set of restraints for each individual
466 structure was then generated as the average and standard deviation of the ρ_C and ρ_N with the
467 top CC score, and all those with at least 95% of that score (Fig. S9). A detailed description of
468 these and other analysis procedures can be found in Supplementary Methods.

469

470 ***In crystallo* UV/Vis absorption spectroscopy**

471 *In crystallo* UV/Vis absorption spectroscopy was performed at the ID29S-Cryobench
472 Laboratory, ESRF, Grenoble, France⁶⁷. Here, crystals were treated as for the steady-state XFEL
473 experiments (see above) to photoreduce them into the different redox states. Samples were then
474 directly mounted on the Cryobench goniometer at 100 K under constant nitrogen gas flow. All
475 data was acquired with a 25 µm focal point for the probing white light beam, while the detector
476 optics was connected to the outgoing objective via a 200 µm-diameter optical fiber. Individual
477 acquisition times were 200 ms, with ten acquisitions being averaged per spectrum.

478

479

480 **References**

481

482 1. Belevich, I., Bloch, D. A., Belevich, N., Wikström, M. & Verkhovsky, M. I. Exploring the
483 proton pump mechanism of cytochrome c oxidase in real time. *Proceedings of the*
484 *National Academy of Sciences of the United States of America* **104**, 2685–2690 (2007).

485 2. Field, C. B., Behrenfeld, M. J., Randerson, J. T. & Falkowski, P. Primary production of
486 the biosphere: Integrating terrestrial and oceanic components. *Science* **281**, 237–240
487 (1998).

488 3. Sun, F. *et al.* Crystal structure of mitochondrial respiratory membrane protein
489 Complex II. *Cell* **121**, 1043–1057 (2005).

490 4. Alberts, B. *et al.* Electron-Transport Chains and Their Proton Pumps. (2002).

491 5. Nicholls, D. G. & Ferguson, S. J. Respiratory Chains. in *Bioenergetics* 91–157 (Elsevier,
492 2013). doi:10.1016/b978-0-12-388425-1.00005-1.

493 6. Entsch, B. & Ballou, D. P. Flavins. in *Encyclopedia of Biological Chemistry: Second*
494 *Edition* 309–313 (Elsevier Inc., 2013). doi:10.1016/B978-0-12-378630-2.00014-1.

495 7. Wang, J., Du, X., Pan, W., Wang, X. & Wu, W. Photoactivation of the
496 cryptochrome/photolyase superfamily. *Journal of Photochemistry and Photobiology C:*
497 *Photochemistry Reviews* **22**, 84–102 (2015).

498 8. Kao, Y. T. *et al.* Ultrafast dynamics of flavins in five redox states. *Journal of the*
499 *American Chemical Society* **130**, 13132–13139 (2008).

500 9. Liu, Z. *et al.* Determining complete electron flow in the cofactor photoreduction of
501 oxidized photolyase. *Proceedings of the National Academy of Sciences* **110**, 12966–
502 12971 (2013).

503 10. Müller, P., Ignatz, E., Kiontke, S., Brettel, K. & Essen, L. O. Sub-nanosecond tryptophan
504 radical deprotonation mediated by a protein-bound water cluster in class II DNA
505 photolyases. *Chemical Science* **9**, 1200–1212 (2018).

506 11. Nohr, D. *et al.* Extended Electron-Transfer in Animal Cryptochromes Mediated by a
507 Tetrad of Aromatic Amino Acids. *Biophysical Journal* **111**, 301–311 (2016).

- 508 12. Aubert, C., Vos, M. H., Mathis, P., Eker, A. P. & Brettel, K. Intraprotein radical transfer
509 during photoactivation of DNA photolyase. *Nature* **405**, 586–590 (2000).
- 510 13. Sancar, A. Mechanisms of DNA Repair by Photolyase and Excision Nuclease (Nobel
511 Lecture). *Angewandte Chemie - International Edition* **55**, 8502–8527 (2016).
- 512 14. Zhong, D. Electron Transfer Mechanisms of DNA Repair by Photolyase. *Annual Review*
513 *of Physical Chemistry* **66**, 691–715 (2015).
- 514 15. Zhao, X. *et al.* Reaction mechanism of (6-4) photolyase. *Journal of Biological Chemistry*
515 **272**, 32580–32590 (1997).
- 516 16. Zhang, M., Wang, L. & Zhong, D. Photolyase: Dynamics and electron-transfer
517 mechanisms of DNA repair. *Archives of Biochemistry and Biophysics* **632**, 158–174
518 (2017).
- 519 17. Chaves, I. *et al.* The Cryptochromes: Blue Light Photoreceptors in Plants and Animals.
520 *Annual Review of Plant Biology* **62**, 335–364 (2011).
- 521 18. Sancar, A. & Zhong, D. It is chemistry but not your grandfather's chemistry.
522 *Biochemistry* **56**, 1–2 (2017).
- 523 19. Brettel, K. & Byrdin, M. Reaction mechanisms of DNA photolyase. *Current Opinion in*
524 *Structural Biology* **20**, 693–701 (2010).
- 525 20. Müller, F. Flavin radicals: Chemistry and biochemistry. *Free Radical Biology and*
526 *Medicine* **3**, 215–230 (1987).
- 527 21. Balland, V., Byrdin, M., Eker, A. P. M., Ahmad, M. & Brettel, K. What Makes the
528 Difference between a Cryptochrome and DNA Photolyase? A Spectroelectrochemical
529 Comparison of the Flavin Redox Transitions. *Journal of the American Chemical Society*
530 **131**, 426–427 (2009).
- 531 22. Park, H., Kim, S., Sancar, A. & Deisenhofer, J. Crystal structure of DNA photolyase from
532 *Escherichia coli*. *Science* **268**, 1866–1872 (1995).
- 533 23. Kiontke, S. *et al.* Crystal structures of an archaeal class II DNA photolyase and its
534 complex with UV-damaged duplex DNA. *The EMBO journal* **30**, 4437–49 (2011).
- 535 24. Mees, A. *et al.* Crystal structure of a photolyase bound to a CPD-like DNA lesion after
536 in situ repair. *Science* **306**, 1789–1793 (2004).
- 537 25. Kort, R., Komori, H., Adachi, S. I., Miki, K. & Eker, A. DNA apophotolyase from *Anacystis*
538 *nidulans*: 1.8 Å structure, 8-HDF reconstitution and X-ray-induced FAD reduction. *Acta*
539 *Crystallographica Section D: Biological Crystallography* **60**, 1205–1213 (2004).
- 540 26. Chapman, H. N. *et al.* Femtosecond X-ray protein nanocrystallography. *Nature* **470**,
541 73–78 (2011).
- 542 27. Neutze, R. & Moffat, K. Time-resolved structural studies at synchrotrons and X-ray free
543 electron lasers: Opportunities and challenges. *Current Opinion in Structural Biology*
544 vol. 22 651–659 (2012).
- 545 28. Spence, J. C. H. XFELs for structure and dynamics in biology. *IUCrJ* **4**, 322–339 (2017).

- 546 29. Coquelle, N. *et al.* Chromophore twisting in the excited state of a photoswitchable
547 fluorescent protein captured by time-resolved serial femtosecond crystallography.
548 *Nature Chemistry* **10**, 31–37 (2018).
- 549 30. Nango, E. *et al.* A three-dimensional movie of structural changes in bacteriorhodopsin.
550 *Science* **354**, 1552–1557 (2016).
- 551 31. Nogly, P. *et al.* Retinal isomerization in bacteriorhodopsin captured by a femtosecond
552 x-ray laser. *Science* **361**, (2018).
- 553 32. Tenboer, J. *et al.* Time-resolved serial crystallography captures high-resolution
554 intermediates of photoactive yellow protein. *Science* **346**, 1242–1246 (2014).
- 555 33. Skopintsev, P. *et al.* Femtosecond-to-millisecond structural changes in a light-driven
556 sodium pump. *Nature* **583**, 314–318 (2020).
- 557 34. Kupitz, C. *et al.* Serial time-resolved crystallography of photosystem II using a
558 femtosecond X-ray laser. *Nature* **513**, 261–265 (2014).
- 559 35. Pande, K. *et al.* Femtosecond structural dynamics drives the trans/cis isomerization in
560 photoactive yellow protein. *Science (New York, N.Y.)* **352**, 725–9 (2016).
- 561 36. Schmidt, M. Time-resolved macromolecular crystallography at pulsed X-ray sources.
562 *International Journal of Molecular Sciences* vol. 20 1401 (2019).
- 563 37. Rould, M. A. & Carter, C. W. Isomorphous Difference Methods. *Methods in*
564 *Enzymology* **374**, 145–163 (2003).
- 565 38. Nakai, S., Yoneda, F. & Yamabe, T. Theoretical study on the lowest-frequency mode of
566 the flavin ring. *Theoretical Chemistry Accounts* **103**, 109–116 (1999).
- 567 39. Fox, K. M. & Karplus, P. A. Old yellow enzyme at 2 Å resolution: overall structure,
568 ligand binding, and comparison with related flavoproteins. *Structure (London,*
569 *England : 1993)* **2**, 1089–105 (1994).
- 570 40. Lennon, B. W., Williams, C. H. & Ludwig, M. L. Crystal structure of reduced thioredoxin
571 reductase from *Escherichia coli*: Structural flexibility in the isoalloxazine ring of the
572 flavin adenine dinucleotide cofactor. *Protein Science* **8**, 2366–2379 (2008).
- 573 41. White, T. A., Johnson, W. H., Whitman, C. P. & Tanner, J. J. Structural basis for the
574 inactivation of *Thermus thermophilus* proline dehydrogenase by N-propargylglycine.
575 *Biochemistry* **47**, 5573–5580 (2008).
- 576 42. Draper, R. D. & Ingraham, L. L. A potentiometric study of the flavin semiquinone
577 equilibrium. *Archives of Biochemistry and Biophysics* **125**, 802–808 (1968).
- 578 43. Wijaya, I. M. M., Domratheva, T., Iwata, T., Getzoff, E. D. & Kandori, H. Single
579 Hydrogen Bond Donation from Flavin N5 to Proximal Asparagine Ensures FAD
580 Reduction in DNA Photolyase. *Journal of the American Chemical Society* **138**, 4368–
581 4376 (2016).
- 582 44. Iwata, T., Zhang, Y., Hitomi, K., Getzoff, E. D. & Kandori, H. Key dynamics of conserved
583 asparagine in a cryptochrome/photolyase family protein by Fourier transform infrared
584 spectroscopy. *Biochemistry* **49**, 8882–8891 (2010).

- 585 45. Ludwig, M. L., Schopfer, L. M., Metzger, A. L., Patridge, K. A. & Massey, V. Structure
586 and Oxidation-Reduction Behavior of 1-Deaza-FMN Flavodoxins: Modulation of Redox
587 Potentials in Flavodoxins. *Biochemistry* **29**, 10364–10375 (1990).
- 588 46. Walsh, J. D. & Miller, A. F. Flavin reduction potential tuning by substitution and
589 bending. *Journal of Molecular Structure: THEOCHEM* **623**, 185–195 (2003).
- 590 47. Domratcheva, T. Neutral histidine and photoinduced electron transfer in DNA
591 photolyases. *Journal of the American Chemical Society* **133**, 18172–18182 (2011).
- 592 48. Dereka, B. *et al.* Direct Observation of a Photochemical Alkyne-Allene Reaction and of
593 a Twisted and Rehybridized Intramolecular Charge-Transfer State in a Donor-Acceptor
594 Dyad. *Journal of the American Chemical Society* **139**, 16885–16893 (2017).
- 595 49. Kao, Y.-T. *et al.* Ultrafast Dynamics and Anionic Active States of the Flavin Cofactor in
596 Cryptochrome and Photolyase. *Journal of the American Chemical Society* **130**, 7695–
597 7701 (2008).
- 598 50. Damiani, M. J., Nostedt, J. J. & O'Neill, M. A. Impact of the N5-proximal Asn on the
599 thermodynamic and kinetic stability of the semiquinone radical in photolyase. *The*
600 *Journal of biological chemistry* **286**, 4382–91 (2011).
- 601 51. Berndt, A. *et al.* A novel photoreaction mechanism for the circadian blue light
602 photoreceptor Drosophila cryptochrome. *Journal of Biological Chemistry* **282**, 13011–
603 13021 (2007).
- 604 52. Mowat, C. G. *et al.* Kinetic and crystallographic analysis of the key active site acid base
605 arginine in a soluble fumarate reductase. *Biochemistry* **40**, 12292–12298 (2001).
- 606 53. Senger, M. *et al.* How FeFe-Hydrogenase Facilitates Bidirectional Proton Transfer.
607 *Journal of the American Chemical Society* **141**, 17394–17403 (2019).
- 608 54. Stevens, D. R. & Hammes-Schiffer, S. Examining the Mechanism of Phosphite
609 Dehydrogenase with Quantum Mechanical/Molecular Mechanical Free Energy
610 Simulations. *Biochemistry* **59**, 943–954 (2020).
- 611 55. van der Kamp, M. W., Perruccio, F. & Mulholland, A. J. High-level QM/MM modelling
612 predicts an arginine as the acid in the condensation reaction catalysed by citrate
613 synthase. *Chemical Communications* 1874–1876 (2008) doi:10.1039/b800496j.
- 614 56. Keenholz, R. A. *et al.* Arginine as a general acid catalyst in serine recombinase-
615 mediated DNA cleavage. *Journal of Biological Chemistry* **288**, 29206–29214 (2013).
- 616 57. Paddock, M. L. *et al.* ENDOR spectroscopy reveals light induced movement of the H-
617 bond from Ser-L223 upon forming the semiquinone (QB-•) in reaction centers from
618 Rhodospirillum rubrum. *Biochemistry* **46**, 8234–8243 (2007).
- 619 58. Sugahara, M. *et al.* Grease matrix as a versatile carrier of proteins for serial
620 crystallography. *Nature Methods* **12**, 61–63 (2014).
- 621 59. Yabashi, M., Tanaka, H. & Ishikawa, T. free-electron lasers Overview of the SACLA
622 facility. *J. Synchrotron Rad* **22**, 477–484 (2015).

- 623 60. Nakane, T. *et al.* Data processing pipeline for serial femtosecond crystallography at
624 SACLA. *Journal of Applied Crystallography* **49**, 1035–1041 (2016).
- 625 61. White, T. A. *et al.* CrystFEL : a software suite for snapshot serial crystallography.
626 *Journal of Applied Crystallography* **45**, 335–341 (2012).
- 627 62. Winn, M. D. *et al.* Overview of the CCP4 suite and current developments. *Acta*
628 *crystallographica. Section D, Biological crystallography* **67**, 235–42 (2011).
- 629 63. Genick, U. K. *et al.* Structure of a Protein Photocycle Intermediate by Millisecond
630 Time-Resolved Crystallography. *Science* **275**, 1471–1475 (1997).
- 631 64. Carrillo, M. *et al.* High-resolution Crystal Structures of Transient Intermediates in the
632 Phytochrome Photocycle. *Structure* 2020.09.16.298463 (2021)
633 doi:10.1101/2020.09.16.298463.
- 634 65. Claesson, E. *et al.* The primary structural photoresponse of phytochrome proteins
635 captured by a femtosecond x-ray laser. *eLife* **9**, (2020).
- 636 66. Afonine, P. v. *et al.* Towards automated crystallographic structure refinement with
637 *phenix.refine*. *Acta Crystallographica Section D Biological Crystallography* **68**, 352–367
638 (2012).
- 639 67. von Stetten, D. *et al.* *In crystallo* optical spectroscopy (*ic* OS) as a complementary tool
640 on the macromolecular crystallography beamlines of the ESRF. *Acta Crystallographica*
641 *Section D Biological Crystallography* **71**, 15–26 (2015).

642

643 **Acknowledgments**

644 The XFEL experiments were performed at the BL2 of SACLA with the approval of the Japan
645 Synchrotron Radiation Research Institute (JASRI) (Proposal No. 2017A8019, 2017B8052,
646 2018A8008, 2018B8031, 2019A8014, 2019B8005). We would like to thank Tzu-Chun Hsiao,
647 and Miu-lun Wu for their assistance in sample preparation. We are also grateful to Tomoyuki
648 Tanaka, Toshi Arima, Yoshinori Matsuura, Hisashi Naitow, Naoki Kunishima, Tetsukon Kin,
649 and the members of Engineering Support Team of SACLA for help during our X-ray
650 experiments, as well as to Takanori Nakane for his introduction to CrystFEL. We thank all staff
651 members of the TPS05A beamline, NSRRC, a national user facility supported by MOST, ROC,
652 and in particular Chien-Chang Tseng and Chung-Kuang Chou for their help in setting up non-
653 standard conditions for crystal testing. Also, Hui-Lin Shr (Crystallization Facility of the
654 Institute of Biological Chemistry, Academia Sinica) provided the location for crystallization
655 under non-standard conditions, which were initially tested with equipment kindly provided by
656 Dr. Shin-Guang Shyu. We would like to thank Dr. Thomas C. Terwilliger (Los Alamos
657 National Laboratory) for his kind help in understanding the theoretical underpinnings of
658 Bayesian difference refinement. We would also like to thank Guillaume Gottthard for his

659 assistance in acquiring the redox-dependent *in crystallo* spectra at the ID29S-Cryobench
660 laboratory, which is a platform of the Grenoble Instruct-ERIC center (ISBG; UMS 3518
661 CNRS-CEA-UGA-EMBL) within the Grenoble Partnership for Structural Biology (PSB).
662 Finally, we would like to thank Mr. Alvaro Maestre Reyna for help in setting up the necessary
663 scripts and macros for calculating extrapolated structure factors.

664

665 **Funding**

666 The work was supported by Academia Sinica and the Taiwan Protein Project funded by MOST
667 (Grant No. AS-KPQ-105-TPP and AS-KPQ-109-TPP2), and in part by JSPS KAKENHI
668 (16K01942). L.O.E. thanks for support by Air Force Office of Scientific Research (AFOSR;
669 Grant No. FA9550-14-1-0409) and German Research Foundation (DFG, Grant No. ES152/18).
670 S.I. acknowledges support by Platform Project for Supporting Drug Discovery and Life
671 Science Research (Basis for Supporting Innovative Drug Discovery and Life Science Research
672 (BINDS)) from Japan Agency for Medical Research and Development (AMED).

673

674 **Author contributions**

675 MMR, SI, LOE, YB, and MDT conceived the research and designed experiments. MMR, CHY,
676 EN, WCH, EPGNP, WJW, PHW, SFB, MS, HJE, HYW, CCL, KFH, YKC, JHL, JHW, WG,
677 CWC, AHP, MS, SO, YH, AY, RT, TT, LF, KT, RS, AR, JY, LOE, and YB performed
678 experiments. MMR, CHY, EN, YJ, SK, IS, LOE, YB, and MDT analyzed the data. MMR,
679 EPGNP, LOE, and AR performed *in-crystallo* spectroscopy. MMR and CHY established and
680 analyzed the multiple refinement approach protocol. KCH performed structure-based PDB
681 search. MMR, WJW, CHY, [AR](#), LOE, YB, and MDT wrote the manuscript.

682

683 **Additional information**

684 Supplementary information is available in the online version of the paper. Correspondence and
685 requests for materials should be addressed to Ming-Daw Tsai. Structural models, along with
686 structure factors presented here can be found under PDB accession codes [7F8T](#), [6LT3](#), [6LT1](#),
687 [6LT2](#), [6LM4](#), [6LMB](#), [6LM5](#), [6LM6](#), [6LM7](#), [6LM8](#), [6LMC](#), [6LM9](#), [6LME](#), [6LMA](#), [7CLW](#),
688 [7C3P](#), [7C3R](#), [7C3W](#), [7C3X](#), [7CLM](#), [7CLN](#), [7CLO](#), [7CLP](#), and [7CLQ](#).

689

690 **Competing financial interests**

691 The authors declare no conflict of financial interest.